PAPER

Polytriphenylamine composites for energy storage electrodes: effect of pendant *vs.* backbone polymer architecture of the electroactive group†

Afshin Dianatdar, [ID] [a] Okan Akin,[a] Irene Mongatti,[a] Jamo Momand, [ID] [b]
Giacomo Ruggeri,[c] Francesco Picchioni[a] and Ranjita K. Bose [ID] *[a]

Polymers are an increasingly used class of materials in semiconductors, photovoltaics and energy storage. Polymers bearing triphenylamine (TPA) or its derivatives in their structures have shown promise for application in electrochemical energy storage devices. The aim of this work is to systematically synthesize polymers bearing TPA units either as pendant groups or directly along the backbone of the polymer and evaluate their performance as electrochemical energy storage electrode materials. The first was obtained *via* radical polymerization of an acrylate monomer bearing TPA as a side group, resulting in a non-conjugated polymer with individual redox active sites (rP). The latter was obtained by oxidative polymerization of a substituted TPA, resulting in a conjugated polymer with TPA units along its backbone (cP). These polymers were then developed into electrodes by separately blending them with multi-wall carbon nanotubes (rC and cC). The electrodes were characterized and their charge storage stability and mechanical properties were investigated for up to 1000 cycles by cyclic voltammetry, galvanostatic charge–discharge measurements and nanoindentation. The results show that cC offers a higher initial charge capacity than rC as well as improved carbon nanotube dispersion due to its conjugated structure. Although the improved dispersion results in a higher elastic modulus for cC (compared to rC), the stiffer nature of cP made it more vulnerable to degrade upon repetitive volumetric change, while with rP, the decoupled acrylate monomer remained more protected when its redox active units of TPA underwent charge–discharge cycling.

Introduction

Electroactive polymers have attracted a lot of interest in electrochemical energy storage devices in the past two decades, stretching the realm of conventional inorganic materials with organic (macro)molecules. Fast electrochemical kinetics, good charge–discharge capacity, mechanical flexibility, resource availability, and being comparably cheaper and more environmentally friendly are among the reasons making them a desirable choice.[1–5]

Among electroactive polymers, the ones that bear triphenylamine (TPA) groups in their structure have gained special interest. The promising performance of TPA-bearing polymers (PTPAs) is attributed to the chemical structure of TPA,

combining the conductivity of poly(*p*-phenylene) with high energy density of polyaniline.[6] In an early study, Feng *et al.*[6] reported that a PTPA derivative showed a high capacity of 103 mA h g^{−1}, when used as a battery cathode and cycled at 0.5C. Following this, there were multiple reports on application of PTPAs in batteries or supercapacitors. The main focus has been increasing of electrode capacity as well as power/energy density by structural tuning of TPA and/or its combination with inorganic materials.[7–18] Despite this progress, the long-term performance and stability of PTPAs can be a bottleneck toward their practical applications, like other electroactive polymers.[19–22] This stability issue arises from the repetitive insertion/disinsertion of counter ions during charge–discharge cycles, resulting in a constant volumetric change. Such an event culminates in mechanical disintegration and performance loss during time.[23–25] This problem could be exacerbated with rod-like rigid structure of conjugated polymers,[26–28] which are significantly stiffer than the traditional flexible polymers.

To tackle the above challenge, it is crucial to have an understanding how the structure of PTPA is impacted when oxidized/reduced during a charge/discharge cycle. Despite different derivatives of PTPAs,[6,13,16,29] they could be broadly categorized into two groups: (i) the ones in which the TPA also

[a]Department of Chemical Engineering, Engineering and Technology Institute Groningen (ENTEG), University of Groningen, Nijenborgh 4, 9747AG Groningen, The Netherlands. E-mail: r.k.bose@rug.nl; Tel: +31 50 3634486

[b]Zernike Institute for Advanced Materials, University of Groningen, Nijenborgh 4, 9747AG Groningen, The Netherlands

[c]Dipartimento di Chimica e Chimica Industriale, Università di Pisa, Via G. Moruzzi 13, 56124 Pisa, Italy

† Electronic supplementary information (ESI) available. See DOI: 10.1039/d1ra06415k

serve as the building block with placing TPA along the polymer backbone; (ii) the ones with TPA decoupled from the backbone, placing it in side chain of the building block (see Scheme 1). The first one makes a conjugated PTPA, while the latter is a non-conjugated but redox active PTPA.

The advantage of conjugated PTPAs can be a higher conductivity; though when a TPA unit is oxidized, it may limit the doping level by hindering oxidation of the adjacent TPA unit. On the other hand, redox PTPAs could be fully doped and have shown to have lower Coulombic repulsion.[30–32] From mechanical stability point of view, it could be hypothesized that a conjugated PTPA is more severely affected as its backbone undergoes constant volumetric change.

At the same time, it should be noted that electroactive polymers (conjugated or redox-active) have rarely been singularly used as an electrode. They are often combined with other highly conductive fillers to meet the requirement of high bulk conductivity in an electrode which is necessary for fast electron transfer. A common choice is carbon-based nanomaterials, which also offer additional mechanical protection to electroactive polymers when combined with them.[33,34] Carbon nanotube (CNT) can be particularly attractive as an strengthening filler[7] due to their high electrical conductivity and mechanical strength.[7] In these applications, polymers could be either covalently or non-covalently hybridized with CNTs.[35] While the former results in a more intimate contact between polymer and the nanotube, the sp² hybridized structure of CNT is disturbed during the polymer–CNT "grafting process", undermining the electronic performance of the composite.[36,37] On the other hand, a non-covalent processing of electroactive polymer with nanotube often relies on π–π stacking and/or hydrogen bonding between the polymer and CNT, which could preserve the primary properties of CNT and benefit from their synergistic effects.[38] Nevertheless, for the current discussion, an important question is how CNTs interact with either conjugated PTPA or redox PTPA in polymer-wrapped CNTs *via* non-covalent approach. This particular aspect has never been explored, which we systematically explore with this research.

Two sets of polymers were synthesized: one with TPA units as side groups representative of redox PTPA (hereafter called as rP), and the other with TPA units along its backbone representative of a conjugated PTPA (hereafter called as cP). Both sets

were fully characterized and their electrochemical properties were studied. They were then further processed with CNTs to make composites (rC and cC, respectively). Subsequently, their energy storage performance was monitored through charge–discharge experiments and mechanical tests up to 1000 cycles.

It should be noted that the aim of this work was to investigate the fundamental question of how differences in pendant group *vs.* backbone placement of PTPA in the polymer architecture would impact the electrochemical energy storage performance and stability during repetitive charge–discharge processes.

Experimental

Triphenylamine (98%), phosphorus(v) oxychloride (99%), sodium borohydride (96%), sodium acetate (99%), triethylamine (anhydrous, 99.5%), acryloyl chloride, sodium acetate, 2,2′-azobis(2-methylpropionitrile) (AIBN, 98%), 4-methoxytriphenylamine (97%), iron(III) chloride (97%), *N,N*-dimethylformamide (DMF, 99.8%), methyl alcohol (99.8%), 1-methyl-2-pyrrolidinone (NMP, 99%) and anhydrous chloroform (99%) were all purchased from Sigma Aldrich and used as received. Tetrahydrofuran (Boom) and toluene (Macron) were dried using the MBraun SPS800 system. Carboxylic-acid functionalized multiwall carbon nanotube (MWCNT-COOH, 9.5 nm × 1.5 micron) was also purchased from Aldrich and used with no further treatment.
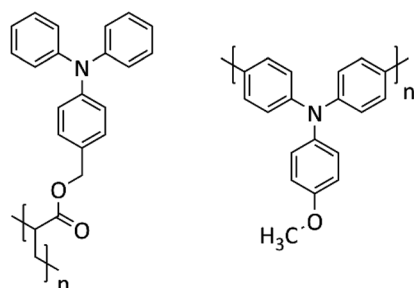
Synthesis of TPAA monomer

The monomer was synthesized in three steps (Scheme 2) using established procedures[39] with the following modifications.

4-(Diphenylamino)benzaldehyde (TPA-CHO). In step one, following Vilsmeier Haack Formylation, phosphorus oxychloride (19.05 mL) was added to (58 mL) dry DMF at 0 °C and the solution was stirred gently under inert atmosphere for 15 minutes until Vilsmeier reagent was formed. Subsequently, TPA (50 g) and additional solvent (150 mL) were added to the reaction flask, and the reaction mixture was stirred at 80 °C for 6 hours. Then the reaction solution was cooled to ambient temperature and added in several portions into a mixture of ice water solution and sodium acetate (37.5 g) and stirred vigorously for several minutes. The precipitated solid was collected by centrifugation and washed several times with deionized (DI) water till a dark yellow (to muddy) material was obtained. Column chromatography (toluene : hexane 4 : 1) resulted in a yellow powder of TPA-CHO.

^{1}*H-NMR (400 MHz, CDCl₃).* δ ppm = 9.81 (s, 1H, CHO), 7.68 (d, J = 8.8 Hz, 2H, H–Ar), 7.34 (t, J = 7.9, 4H, H–Ar), 7.18–7.15 (m, 6H, H–Ar), 7.01 (d, J = 8.7 Hz, 2H, H–Ar) (Fig. S1†).

^{13}*C-NMR (MHz, CDCl₃).* δ ppm = 193.2 (s, 1C), 156.0 (s, 1C), 148.9 (s, 2C), 134.0 (s, 2C), 132.4 (s, 4C), 131.7 (s, 1C), 129.0 (s, 2C), 127.7 (s, 4C), 122.0 (s, 2C) (Fig. S1†).

[4-(*N*-Phenylanilino)phenyl] methanol (TP-CH₂OH). In step 2, TPA-CHO (20 g) was dissolved in a dry mixture of toluene : methanol (50 : 50% v/v) at 0 °C, and excess NaBH₄ (5 g) was gradually added to the flask under inert atmosphere. The

Scheme 1 TPA-polymer architecture with TPA in side chain (left), and along the backbone (right).
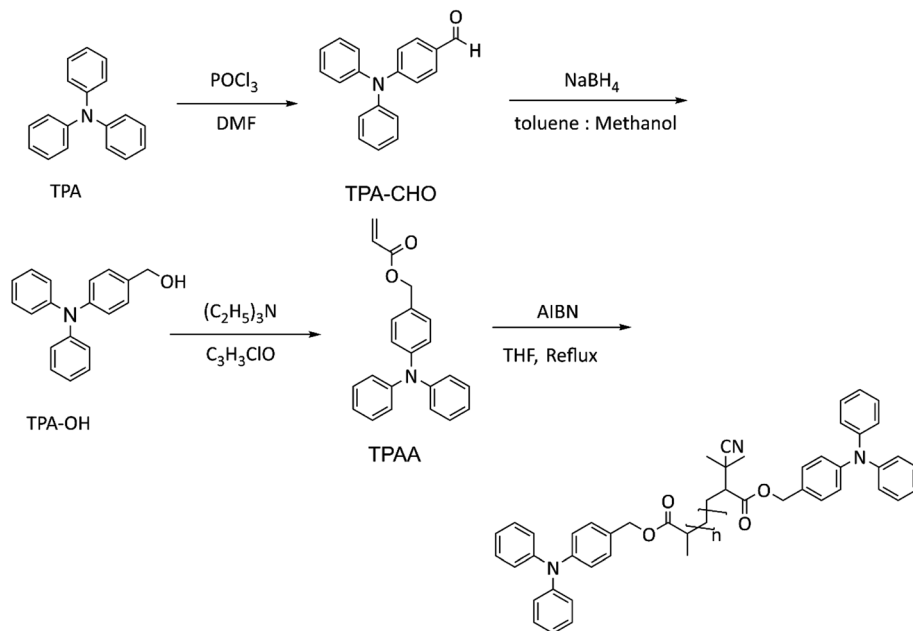
Scheme 2 Synthesis of TPAA and its radical polymerization to rP.

reaction continued for 5 h at 0 °C and at RT overnight. Then the solvent was evaporated using a rotary evaporator, and the crude product was washed and extracted several times with DCM and DI water. The organic layer was dried over $MgSO_4$, and solvent was evaporated using a rotary evaporator. White TPA-CH_2O was recrystallized at RT in a few hours. The alcohol was dried in a vacuum oven before using in step 3.

^{1}H-NMR (400 MHz, CDCl$_3$). δ ppm = 7.29–7.20 (m, 6H, H–Ar), 7.08 (pd, *J* = 7.84, 6H, H–Ar), 7.01 (t, *J* = 7.32, 2H, H–Ar), 4.63 (s, 2H, –CH$_2$–), 1.68–1.54 (m, 1H, –OH) (Fig. S2†).

^{13}C-NMR (MHz, CDCl$_3$). δ ppm = 150.4 (s, 1C), 150.1(s, 2C), 137.6 (s, 1C), 131.8 (s, 4C), 130.9 (s, 2C), 126.9 (s, 6C), 125.4 (s, 2C), 67.8 (s, 1C) (Fig. S2†).

[4-(Diphenylamino)phenyl] methyl ester (TPAA). In step 3, TPA-CH_2OH (15 g) and trimethylamine (45 mL) were added to dry THF (100 mL) under mechanical stirring under inert atmosphere at 0 °C. After a few minutes, 15 mL acryloyl chloride dissolved in THF (50 mL) was added gradually (over 1 h) to the reaction mixture. The reaction was kept at 0 °C for 2 h followed by at RT overnight. The viscous mixture was then diluted with excess of THF and insoluble precipitated salt was removed using 0.2 μm PTFE by vacuum filtration. After solvent evaporation, the crude product was purified using column chromatography (benzene : hexane 67 : 33 to 100 : 0). The white powder was dried in a vacuum oven at 40 °C for 48 h.

^{1}H-NMR (400 MHz, CDCl$_3$). δ ppm = 7.36 (s, 2H), 7.28–7.22 (m, 5H), 7.08–6.98 (m, 7H), 6.48–6.42 (m, 1H), 6.21–6.14 (m, 1H), 6.86–6.83 (m, 1H), 5.12 (s, 2H) (Fig. S3†).

^{13}C-NMR (MHz, CDCl$_3$). δ ppm = 171.5 (s, 1C), 150.6 (s, 1C), 150.2 (s, 2C), 133.7 (s, 2C), 132.2 (s, 4C), 131.9 (s, 1C), 131.0 (s, 2C), 127.1 (s, 2C), 126.0 (s, 4C), 125.7 (s, 2C), 68.8 (s, 1C) (Fig. S3†).

Polymerization

rP. The radical polymerization of TPAA monomer (Scheme 2) was carried out according to established procedures.[40] The monomer (3 mmol) and AIBN (0.15 mmol) were added to a 25 mL three-neck flask charged with anhydrous THF (5 mL), and the mixture was degassed for 45 minutes at 0 °C. The polymerization was then initiated by placing the reaction vessel into an oil bath under reflux temperature till the reaction could no longer progress as a result of increased viscosity (>12 hours). The crude product was diluted with CH_2Cl_2 (2 mL), and followed by precipitation on 100 mL of cold MeOH with gentle stirring. The precipitate was collected by centrifugation, and purification was repeated three times. This resulted in polymer range molar mass (GPC : M_n = 3200, PDI = 1.60). The polymer was dried in a vacuum oven at 60 °C for 24 h before use.

cP. The oxidative polymerization (Scheme 2) was conducted according to ref. 41 with some modifications. Briefly, 4 g of TPA-Me and 9.4 g FeCl$_3$ were added to 20 mL of anhydrous chloroform and degassed for 30 minutes with argon. The reaction vessel was heated under reflux temperature for 24 h. The reaction was quenched with liquid nitrogen, and after returning to room temperature, it was poured onto 700 mL of methanol : HCL(37%) (90 : 10), and the precipitated solid was collected by centrifugation. Then, the solid was dissolved in the minimum amount of chloroform and precipitated onto acetone : ammonia (25%) (90 : 10). The insoluble part was removed using centrifugation, dissolved in THF, filtered through 0.45 mm PTFE and dried at 70 °C overnight (GPC : M_n = 880).

Polymer–CNT composite processing

Two sets of composites, namely the rC and cC were prepared, with ratio of 1 : 1 (polymer : CNT, weight%) (Table 1). In a typical procedure, the relative amounts of CNT and polymer

Table 1 Formulation of polymeric samples and their composites for thin films (for thick films, the numbers should be multiplied by 10)

Sample code	rP (mg)	cP (mg)	CNT (mg)
CNT	—	—	1
rP	1	—	—
rC	1	—	1
cP	—	1	—
cC	—	1	1

were added to solvent (with two concentrations of 0.2 and 2 mg per CNT per mL NMP to obtain thin and thick film, respectively (see below)) and homogenized using an ultrasonic bath for 30–60 minutes. Then the mixture was centrifuged (4500 rpm) to remove large and metallic bundles. The supernatant was used for making composite films and characterization. Neat CNT films were also prepared as reference samples.

Sample preparation

First, all substrates were cleaned by sonicating for 15 minutes in a mixture of soap in DIW, in DIW, in acetone and isopropyl alcohol in four subsequent steps. The substrates were then dried using air pressure. For UV-vis tests, 20 μL of either rP, rC, cP or cC solutions (thin film concentration) was drop-casted onto optical grade quartz (12 × 18 mm^2) and heated at 140 °C for 30 minutes (thin films). For cyclic voltammetry (CV) tests, 100 μL of the solutions (for each concentrations) were drop-casted onto ITO-coated glasses (20 × 15 × 1.1 mm; Ossila, the UK) and heated the same way (thin films). For conductivity and nanoindentation tests, 100 μL of either rP, rC, cP or cC solutions (thick film concentration) was drop-casted onto borosilicate glass (20 × 15 mm) and heated at 140C for 60 minutes.

Characterization

A Varian Mercury Plus 400 (with Varian 5 mm PFG AutoSW probe) was used for ^{1}H NMR. An Agilent MR 400 (with Varian 5 mm OneNMR probe) was used for ^{13}C NMR. A Hewlett Packard 1100 Series with GBC 1240 RID detector and 3× Agilent Technologies PLgel Mixed E column were used for gel permeation chromatography (GPC) using THF (flow of 1 mL min^{-1}) as eluent and polystyrene as reference. A Thermo Spectronic (Thermo Fisher Scientific) was used for spectrophotometry. AFM images were captured in ScanAsyst® mode using a Bruker MultiMode AFM-2. Sample thicknesses were measured using a Bruker Dektak XT profilometer. Conductivity measurements were done using a four-probe resistivity analyzer (T2001A3-EU; Ossila, the UK). Transmission Electron Microscopy (TEM) experiments were performed using a JEOL 2010 operated at 200 kV. Atomic force microscopy (AFM) images were captured in ScanAsyst® mode using a Bruker MultiMode AFM-2. TA Instruments DSC 25 was used for differential scanning calorimetry (DSC) in temperature range 20–200 °C and heating rate of 10 °C min^{-1}.

For cyclic voltammetry (CV) and galvanostatic charge–discharge (GCD) measurements, a three-electrode cell configuration was used. An ITO (Ossila, the UK) coated with sample was used as working electrode (WE), Ag/AgCl (Metrohm) as reference electrode (RE) and platinum sheet (surface = 1 cm^2, Metrohm) as counter electrode (CE) using an Autolab PGSTAT306N potentiostat. Experiments were conducted in an undivided cell in ambient environment with 50 mV s^{-1} scan rate. The electrodes were kept in the same position for each experiment. The results were analyzed using Nova 2.1 software to calculate oxidation and reduction potentials (E_{pa} and E_{pc}) and currents as well as onset potentials. I–V curve was normalized (either by dividing the current to the exposed surface area (for thin films) or electrode mass (thick film) of WE into electrochemical cell. Specific capacity was calculated from galvanostatic charge–discharge experiments as:

$$\text{Specific capacity (mA h g}^{-1}) = I\Delta t/m \qquad (1)$$

where I is the applied current, and m is the mass of active electrode.

Nanoindentation tests were done using a Berkovich indenter in continuous stiffness measurement mode for at least 20 repetitions. The tests were carried out with controlled depth control and force measurement continuously. Hardness is averaged in the range of 200–300 nm and modulus of elasticity is measured at unloading point. Modulus of elasticity is reported at unloading point:[42]

$$H = F/A_r \qquad (2)$$

$$A_r = 24.5h_c \qquad (3)$$

$$h_c = h_{max} - \varepsilon(F_{max}/E) \qquad (4)$$

$$E = \mathrm{d}F/\mathrm{d}h \qquad (5)$$

where H is hardness, F is the applied load and A_r is the residual projected area of contact between the indenter and the specimen in (2); h_c is the measured contact depth in (3); h_{max} is the maximum penetration depth, ε is a constant (0.75 for Berkovich tip) in (4); E is the modulus of elasticity, calculated at the unloading point in (5).

Results and discussion

Polymer–CNT electrode development

The PTPAs (rP and cP) were synthesized (Schemes 2 and 3) and characterized by ^{1}H and ^{13}C NMR and C DEPT NMR (Fig. S4–

TPA-Me → cP
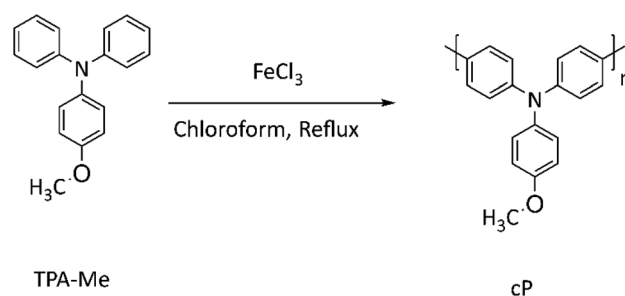
Scheme 3 Oxidation polymerization of TPA-Me to cP.
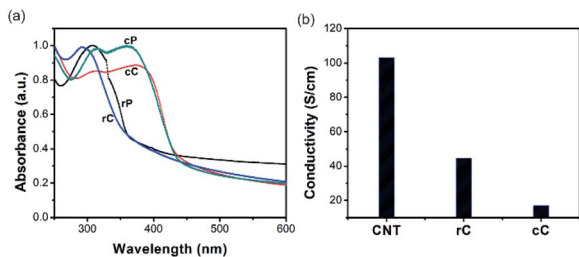
Paper

Fig. 1 (a) UV-vis absorption spectra of rP, cP and their composites with CNTs; (b) surface conductivity of CNT film and polymer composites measured by four-probe resistivity measurement (the values of standard deviation are too low to be observable in the figure).

only a trimer (GPC : M_n = 880). This relatively low molar mass range may be due to a transfer reaction of the growing chain radical on the nitrogen of the TPA, forming a resonance stabilized radical that prevents propagation. Both materials were then separately processed with CNTs to make the polymer–CNT composites of rC and cC. The electronic properties of the polymers and composites were further studied by UV-vis and resistivity measurements (Fig. 1a and b). The absorption spectrum of rP shows a TPA characteristic maximum at 308 nm[40]; which appears at 292 nm for rC. On the other hand, cP shows two absorption bands at 313 and 361 nm, revealing themselves in cC at 313 and 376 nm, respectively.

For polymers, the red-shifting of cP bands compared to rP has been observed previously for poly(4-methoxy-TPA) and was attributed to the extended conjugated length in a typical PTPA backbone.[41] On the other hand, for the composites, the

S7†). For rP, it was possible to obtain polymerization degrees higher than an average of 9 units (GPC : M_n = 3200, PDI = 1.60), while for cP, an extended oxidative polymerization resulted in
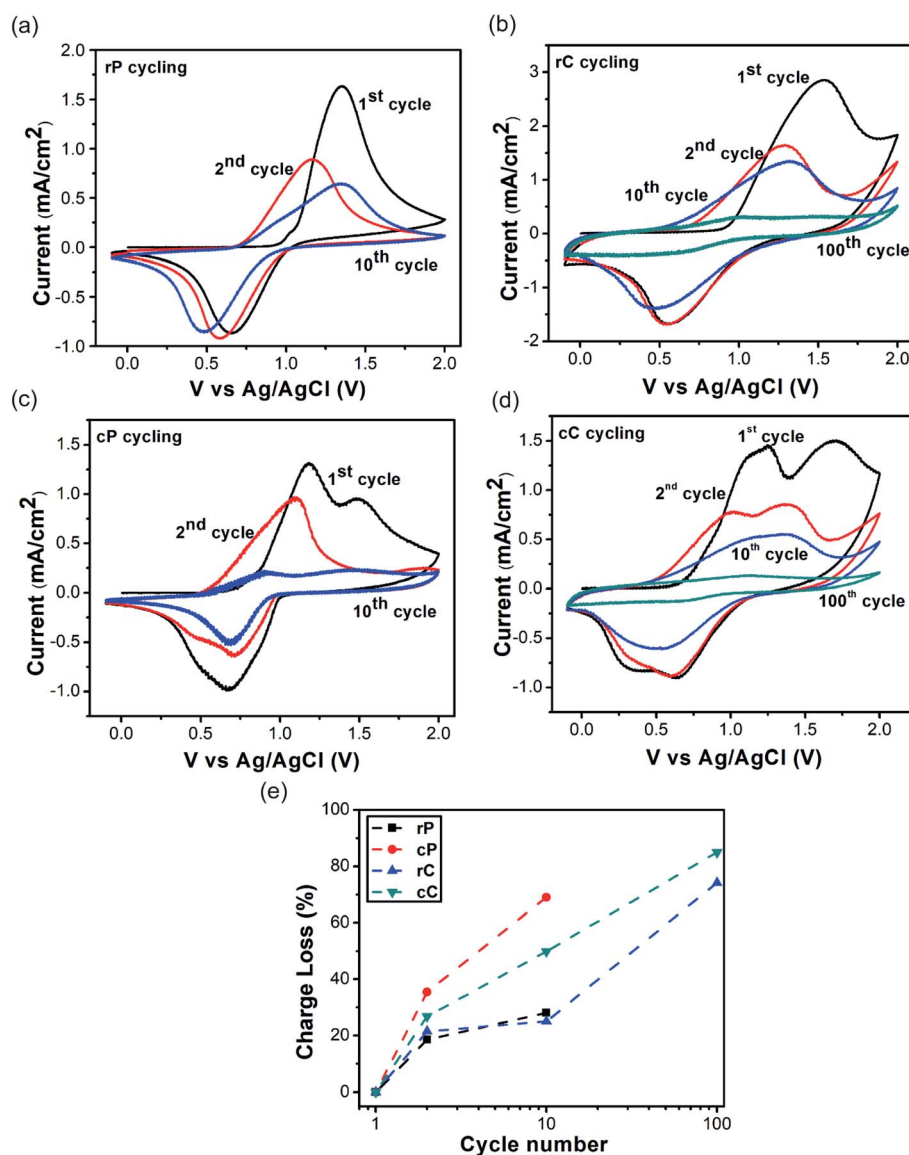

Fig. 2 CV curves of rP, cP and their composite electrodes in 1st, 2nd, 10th, and 100th cycle: (a) rP; (b) rC; (c) cP; (d) cC; (e) their charge loss with cycling. Electrodes are prepared by solution cast of the sample solutions onto ITO. Measurements were performed in 0.1 M TBPO solution in acetonitrile using Ag/AgCl as RE and platinum wire as CE.

absorption band(s) showed a blueshift for rC and a redshift for cC; suggesting a comparably more favorable electronic interaction between cP and CNTs as a result of overlapping orbitals.[43] Fig. 1b shows the conductivity of the CNT film and its composites. Both polymers had a resistivity higher than the threshold of the device (10 M ohm sq^{-1}) for the investigated thickness range (1.5–2 μm). In the composites, the conductivity for rC dropped to less than a half of the value reached by the neat CNT film. This drop, however, is more significant for cC ($\sigma_{rC}/\sigma_{cC} = 2.62$), where σ is the surface conductivity. It could be suggested that rP is facilitating CNTs percolation better than cP due to higher molecular weight ($M_{n\ rP}/M_{n\ cP} = 3.62$), which is in agreement with literature.[44]

Electrochemical characterization

Redox properties. Cyclic voltammetry (CV) of cP, rP, and their composites with CNTs were recorded in acetonitrile/TBAP (0.1 M) using sample-coated ITO as the working electrode (WE), Ag/AgCl as the reference electrode (RE) and platinum as the counter electrode (CE) to study cyclic voltammetry of the samples (Fig. 2a–d).

The Fig. 2a suggests that when rP is first oxidized (TPA to TPA$^{\cdot+}$), the onset oxidation potential is at 1.06 V, which is reduced to 0.76 in the second scan and remains almost unchanged up to 10 cycles. On the other hand, the onset oxidation potential of cP is at 0.86 V, which decreases to 0.52 in the second scan and remains almost the same up to ten cycles (Fig. 2c). Additionally, cP shows two oxidation potential peaks at 1.16 and 1.52. This was observed before and was suggested to be a result of dimerization between two oxidized TPA units (forming TPA–TPA, also called TPB).[45]

For both rC and cC, their onset potentials start at a lower value compared to their constituent polymers (0.93 and 0.71 V, respectively) in the initial scans (as also observed before in redox active polymer–CNT composites).[46] However, from the second scan, both show the same potentials as their polymers. This initial reduction in oxidation potential can be attributed to the synergistic effect between conjugated units of the polymers with CNT walls, encouraging charge transfer, related to the orbital overlapping effect (Fig. 1a). When the oxidation–reduction cycling was continued, it was observed that cP lost its charge capacity (the integration of CV curve) much faster than rP (Fig. 2e). Also, when cP was cycled 10 times, it was observed to delaminate from the surface of the ITO electrode, compared with rP, which preserved its initial electrode integration to the highest extent. In both cases however, CNTs in the composites had a stabilizing effect, which was more pronounced in cP. This is likely due to the interlocking of polymer fragments in the CNT network (Fig. S8a–f†).

Energy storage behavior. To investigate the electrochemical behavior of rC and cC as electrodes in energy storage devices, galvanostatic charge–discharge experiments were performed. In Fig. 2a–d. CVs of the polymers and their composites all show clear peak-to-peak separations. Such irreversible redox reactions are considered a signature of battery-type electrode, different from fully reversible redox reactions suggesting

capacitive like behavior.[47] The current in a battery-like electrode is diffusion-controlled, unlike surface-controlled current response of capacitive-type electrode. As established in literature, the type of current could be investigated with recording of electrode current response at different scan rates:[47]

$$I = aX^b \quad (6)$$

$$\log(I) = \log(a) + b\log(X) \quad (7)$$

where I is the net recorded current and X is the scan rate. It is suggested that b has a value between 0.5 (suggesting diffusion-controlled current) and 1 (suggesting surface-controlled behavior). Clearly, a number between 0.5 and 1 indicates that both surface-controlled and diffusion-controlled response are present.[47,48] Using eqn (6) and (7) and measuring the current responses of the polymers (at oxidation peak (E_{p_a})), the b value for rP is 0.55 and 0.46 for cP (Fig. 3). Therefore, these results suggest diffusion-controlled current response, which is in agreement with the CV data.

Charge–discharge behavior. Typical charge–discharge behaviors of rC and cC are shown in Fig. 4a, b. The current density was varied between 0.5 A g^{-1} to 5 A g^{-1}. This corresponds to a discharge rate of approximately 6C to 60C for rC (with theoretical capacity for rP to be 81 mA h g^{-1}) and 5C to 50C for cC (with theoretical capacity of cP to be 97 mA g^{-1}). Although the range of current densities used in a battery system is much lower, the higher C-rates were chosen to accelerate the electrochemical aging and degradation processes.

The rC discharge (or charge) capacity curve appears to roughly consist of three phases: (i) 1.6–1.1 V, (ii) 1.1–0.75 V and (iii) 0.75–0 V. Among them, the second phase corresponds to a battery-like behavior and the other two phases show fast capacitive response. The discharge curves show an initial capacity of 37 and 44.7 mA h g^{-1} for 6C and 60C, respectively.

For cC on the other hand, the same pattern of three phases was observed but with the extension of "battery region" from 1.1 to 0.5 V. The initial capacity of cC is 28 and 47 mA h g^{-1} for
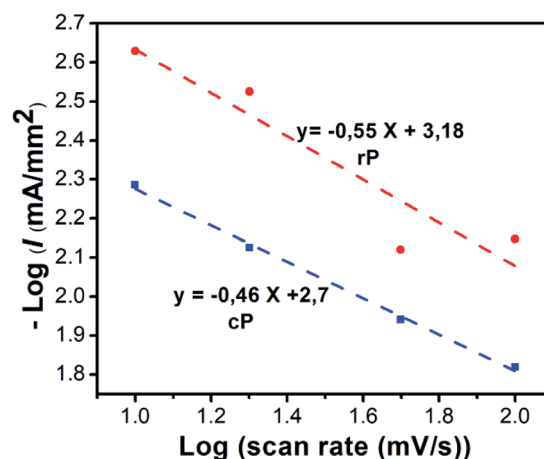

Fig. 3 Current response of rP and cP film electrodes at different scan rates of 10 mV s^{-1}, 20 mV s^{-1}, 50 mV s^{-1}, and 100 mV s^{-1}.
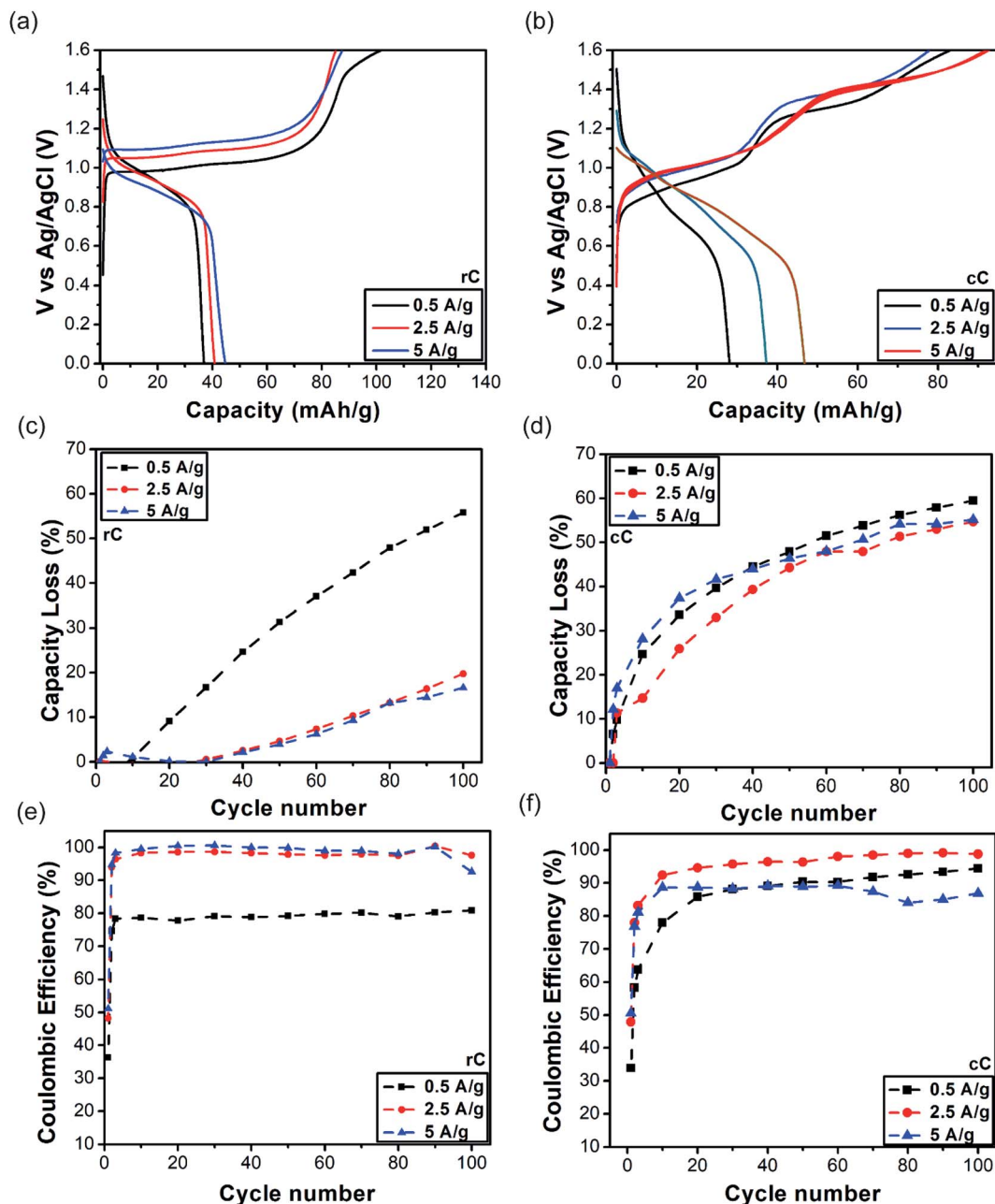
Fig. 4 First scan charge–discharge curves: (a) rC, (b) cC; specific capacity loss during 100 cycle: (c) rC, (d) cC; and coulombic efficiencies: (e) rC, (f) cC.

0.5 A g^{-1} and 5 A g^{-1}, respectively, dropping to 11, and 21 mA h g^{-1} on the 100th cycle (Fig. 5f).

Interestingly in both cases, the higher their discharge C-rate was, the higher their initial capacities became. This is somewhat interesting as the opposite trend has been usually observed and expected in battery electrodes.[13] It is reasoned that when the current density is increased, the capacity would decrease as a result of polarization.[49] Nevertheless, a higher performance at a higher C-rate was further supported with capacity retention and Coulombic efficiency during 100 cycles (Fig. 4c–f). For rC at the discharge rate of 5 A g^{-1}, the capacity
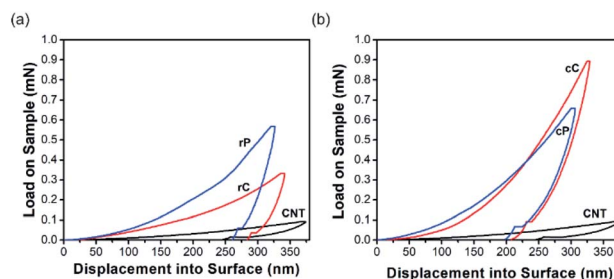

Fig. 5 Nanoindentation curve of (a) rP vs. rC, and (b) cP vs. cC.

loss after 100 cycles is 16% compared to 56% for 0.5 A g^{-1}. On the other hand, these numbers were 55 and 61% for cC at the same current densities. The same effect was observed in the Coulombic efficiencies of the electrodes, though it was more pronounced in the case of rC. These data additionally suggest that rC is a more stable electrode than cC, especially at higher discharge rate. The poorer performance of cC electrode could be a result of material dissolution upon cycling during time (Fig. S8†). This phenomenon is most likely related to the different polarization behavior at nanoscales and/or thin film length scales, which needs further investigation.

Mechanical properties

Nanoindentation in continuous stiffness measurement mode was used for mechanical characterization of thin rP and cP films as well as their composites in micrometer range (Fig. 5). The continuity of all the curves suggest that the films were defect-free within the indentation range.[50] A control sample of interconnected network of CNTs was also tested for comparison.

Calculated from the force – indentation depth curves, the hardness and elastic modulus of CNTs are as low as 26 and 629 MPa, respectively. Both rP and cP show a higher hardness and elastic modulus than CNTs in their pure form; but the increase for cP is slightly higher (Fig. 5a and b). In rC, the hardness decreased from 304 MPa to 125 MPa and modulus of elasticity from 8.98 GPa to 5.51 GPa. However, the trend for cC was exactly the opposite: increasing the hardness from 337 MPa to 544 MPa (61% increase) and elastic modulus from 7.72 GPa to 9.57 GPa (24% increase). This difference in behavior can be attributed to different interaction of CNTs with two polymers at their interfaces. These differences in nanomechanical characterizations of CNT–polymer thin film composites have been reported before. For example, Gupta *et al.*[42] observed that upon adding CNTs in polyurethane, the hardness and elastic modulus of the composite increased up to 271 and 290%, respectively. On the other hand, other reports[51,52] revealed that CNT composites with poly (allylamine hydrochloride) or poly (methyl methacrylate) did not result in significant improvements in mechanical properties. This behavior was attributed to the poor bending strength of CNTs and their easy displacement into the surrounding matrix upon indentation.
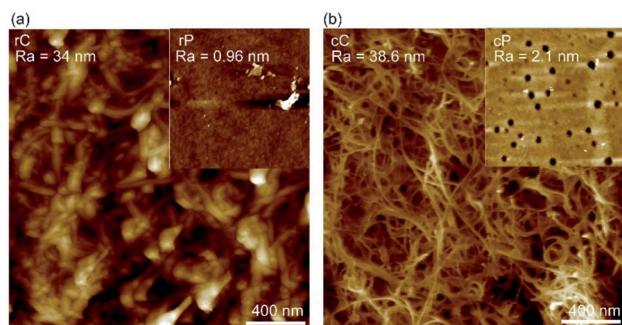
In this work, it should be the inherent nature of cP and rP as well as their interactions with CNTs that result in such a different trend in mechanical properties. Primarily, cP has
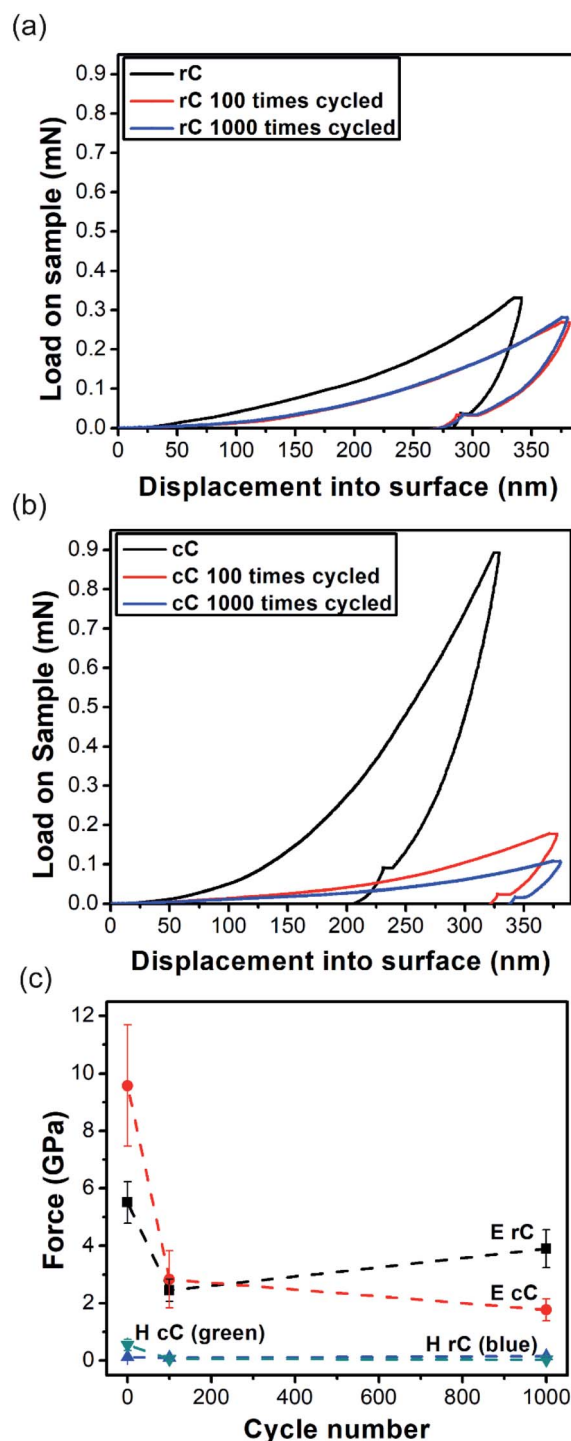

Fig. 7 Indentation curves for (a) rC and (b) cC along with the electrochemically aged samples for 100 cycles (rC/cC 100) and 1000 cycles (rC/cC 1000) of charge−discharge at 5 A g^{-1}; (c) Hardness (*H*) and elastic modulus (*E*) evolution for rC and cC and their aged samples at 5 A g^{-1}. The samples were annealed in an oven at 140 °C for 30 minutes before the test on aged samples to eliminate the effect of solvent.

Fig. 6 AFM of (a) rP and rC; (b) cP and cC.

a higher E and H than rP, suggesting a rigid nature. This is also in line with DSC results showing significant increase of glass transition temperature (180 °C for cP *vs.* 90 °C for rP) (Fig. S10†). On the other hand, AFM suggest that when blended with CNTs, cP is also able to better disperse CNTs (Fig. 6). As a result of these cumulative effects, cC/rC show higher/lower E and H compared to their polymeric constituents.

To investigate the stabilization effect of CNTs on the mechanical properties of the composites upon charge–discharge cycles, both of them were cycled for 100 and 1000 times with 5 A g^{-1} current density and the indentation tests were repeated (Fig. 7a and b). It is clear that the degree of mechanical variation degree in cC upon charge–discharge cycling is more significant compared to rC. Quantifying H and E from eqn (4)–(7), it is concluded that the hardness remained stable for both composites up to 1000 cycles (Fig. 7c); while elastic modulus is significantly decreased for both rC and cC. Yet, the drop in elastic modulus is more pronounced for cC. The stability and morphology of the surface of the electrodes were also studied with AFM scans of the degraded samples (Fig. S11†). We observe that rC could retain more of its initial morphology up to 1000 cycles of charge–discharge when compared with cC. This is most likely related to the observation that the initial dispersion of CNT is compromised in cC and the nanotubes could re-agglomerate. This results also corroborates the charge transfer behavior of the electrodes observed above.

Based on these results, and the morphology of the composites, it can be argued that cP with the TPA unit along its backbone provides steric hindrance between nanotubes, thus restricting their mobility. This avoids dislocation of nanotubes as a result of lower bending strength,[52] while an acrylate backbone in the polymer is unable to prevent the aggregation of the nanotubes. This was further corroborated by TEM (Fig. 8), where cP was able to individualize CNTs more effectively.

However, when the composites are exposed to repetitive oxidation and reduction cycles, the TPA unit at the interface of CNT-cP-CNT is deteriorated resulting in failure at the interface and hence significant loss in elastic modulus. On the other hand, rP has a redox-inactive chain of acrylate, the CNT-rP-CNT could preserve its initial mechanical properties to a higher extent.

Conclusion

Two sets of TPA-electroactive polymers were synthesized (redox and conjugated) and blended with CNTs for studying their application as charge storage electrode materials. The redox and mechanical stability of the composites were investigated. CNTs had a stabilizing effect on capacity retention of both polymers at different scan rates. Yet, the redox PTPA was inherently more stable than the conjugated polymer upon charge–discharge cycling at different current densities. On the other hand, the conjugated PTPA could disperse CNT particles more effectively with stronger π–π interactions, resulting in enhancement of hardness and elastic modulus in their composite. However, when the composites were electrochemically aged by repetitive cycling, the redox polymer could provide a more mechanically stable electrode compared with conjugated polymer by decoupling of the redox-active sites from the polymer backbone. In summary, although the PTPA composites do not show extremely high performance as electrode materials, this work sheds light on the effect of placing the electroactive groups in the polymer backbone *vs.* as pendant group.

The results of this research could be used for the rational design of electrochemical energy storage materials using TPA-based polymers, suggesting a longer lifetime if TPA (derivative) units are decoupled from the backbone. Furthermore, although only TPA has been investigated in this research, the other conjugated monomeric units may potentially follow a similar trend, validation of which needs further research.

Conflicts of interest

The authors state no conflict of interest.

Acknowledgements

Notes and references

1 A. Mauger, C. Julien, A. Paolella, M. Armand and K. Zaghib, *Materials*, 2019, **12**, 1–57.

2 C. Han, J. Zhu, C. Zhi and H. Li, *J. Mater. Chem. A*, 2020, **8**, 15479–15512.

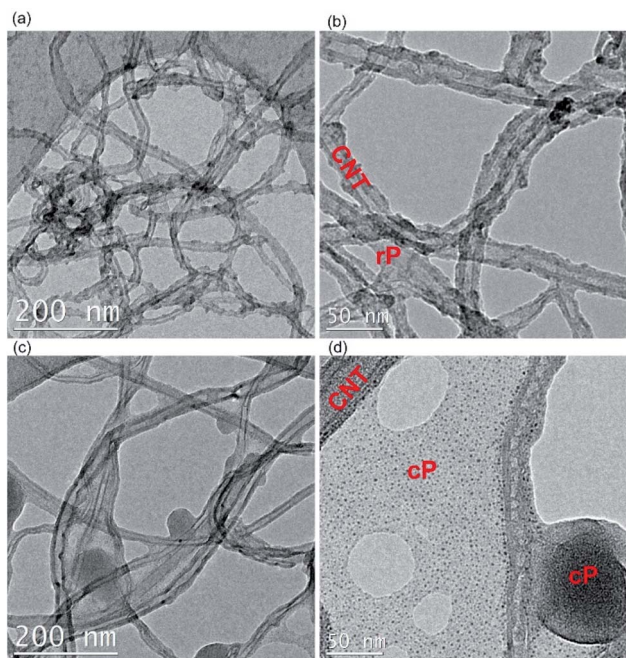3 M. A. Morris, H. An, J. L. Lutkenhaus and T. H. Epps, *ACS Energy Lett.*, 2017, **2**, 1919–1936.

Fig. 8 TEM images of rC (a and b) and cC (c and d).

4   S. Muench, A. Wild, C. Friebe, B. Häupler, T. Janoschka and U. S. Schubert, *Chem. Rev.*, 2016, **116**, 9438–9484.

5   J. Xie, P. Gu and Q. Zhang, *ACS Energy Lett.*, 2017, **2**, 1985–1996.

6   J. K. Feng, Y. L. Cao, X. P. Ai and H. X. Yang, *J. Power Sources*, 2008, **177**, 199–204.

7   C. Su, Y. Ye, X. Bu, L. Xu and C. Zhang, *Adv. Mater. Res.*, 2011, **335–336**, 1512–1515.

8   C. Su, F. Yang, L. Ji, L. Xu and C. Zhang, *J. Mater. Chem. A*, 2014, **2**, 20083–20088.

9   W. Ni, J. Cheng, X. Li, G. Gu, L. Huang, Q. Guan, D. Yuan and B. Wang, *RSC Adv.*, 2015, **5**, 9221–9227.

10 J. Xiong, Z. Wei, T. Xu, Y. Zhang, C. Xiong and L. Dong, *Polymer*, 2017, **130**, 135–142.

11 Z. Peng, X. Yi, Z. Liu, J. Shang and D. Wang, *ACS Appl. Mater. Interfaces*, 2016, **8**, 14578–14585.

12 C. Zhang, X. Yang, W. Ren, Y. Wang, F. Su and J. X. Jiang, *J. Power Sources*, 2016, **317**, 49–56.

13 C. Su, H. He, L. Xu, K. Zhao, C. Zheng and C. Zhang, *J. Mater. Chem. A*, 2017, **5**, 2701–2709.

14 K. Yamamoto, D. Suemasa, K. Masuda, K. Aita and T. Endo, *ACS Appl. Mater. Interfaces*, 2018, **10**, 6346–6353.

15 W. Huang, T. Jia, G. Zhou, S. Chen, Q. Hou, Y. Wang, S. Luo, G. Shi and B. Xu, *Electrochim. Acta*, 2018, **283**, 1284–1290.

16 Z. Chen, W. Li, Y. Dai, N. Xu, C. Su, J. Liu and C. Zhang, *Electrochim. Acta*, 2018, **286**, 187–194.

17 M. E. Roberts, D. R. Wheeler, B. B. McKenzie and B. C. Bunker, *J. Mater. Chem.*, 2009, **19**, 6977–6979.

18 J. T. Kearns and M. E. Roberts, *J. Mater. Chem.*, 2012, **22**, 25447–25452.

19 Q. P. McAllister, K. E. Strawhecker, C. R. Becker and C. A. Lundgren, *J. Power Sources*, 2014, **257**, 380–387.

20 V. Kuznetsov, A. H. Zinn, G. Zampardi, S. Borhani-Haghighi, F. La Mantia, A. Ludwig, W. Schuhmann and E. Ventosa, *ACS Appl. Mater. Interfaces*, 2015, **7**, 23554–23563.

21 M. K. Jangid and A. Mukhopadhyay, *J. Mater. Chem. A*, 2019, **7**, 23679–23726.

22 J. P. Pender, G. Jha, D. H. Youn, J. M. Ziegler, I. Andoni, E. J. Choi, A. Heller, B. S. Dunn, P. S. Weiss, R. M. Penner and C. B. Mullins, *ACS Nano*, 2020, **14**, 1243–1295.

23 R. Koerver, W. Zhang, L. De Biasi, S. Schweidler, A. O. Kondrakov, S. Kolling, T. Brezesinski, P. Hartmann, W. G. Zeier and J. Janek, *Energy Environ. Sci.*, 2018, **11**, 2142–2158.

24 A. Saal, T. Hagemann and U. S. Schubert, *Adv. Energy Mater.*, 2020, 2001984.

25 M. E. Abdelhamid, A. P. O'Mullane and G. A. Snook, *RSC Adv.*, 2015, **5**, 11611–11626.

26 P. Novák, K. Müller, K. S. V. Santhanam and O. Haas, *Chem. Rev.*, 1997, **97**, 207–281.

27 E. Frackowiak, V. Khomenko, K. Jurewicz, K. Lota and F. Béguin, *J. Power Sources*, 2006, **153**, 413–418.

28 Y. Liao, H. Wang, M. Zhu and A. Thomas, *Adv. Mater.*, 2018, **30**, 1705710.

29 J. Xiang, K. Sato, H. Tokue, K. Oyaizu, C. L. Ho, H. Nishide, W. Y. Wong and M. Wei, *Eur. J. Inorg. Chem.*, 2016, **2016**, 1030–1035.

30 Y. Liang, Z. Tao and J. Chen, *Adv. Energy Mater.*, 2012, **2**, 742–769.

31 Z. Qiu, B. A. G. Hammer and K. Müllen, *Prog. Polym. Sci.*, 2020, **100**, 101179.

32 M. Yao, H. Senoh, T. Sakai and T. Kiyobayashi, *J. Power Sources*, 2012, **202**, 364–368.

33 L. Cui, J. Gao, T. Xu, Y. Zhao and L. Qu, *Chem.–Asian J.*, 2016, **11**, 1151–1168.

34 V. Raju, J. V. Rani and P. Basak, *Electrochim. Acta*, 2020, **361**, 137097.

35 Z. Abousalman-Rezvani, P. Eskandari, H. Roghani-Mamaqani and M. Salami-Kalajahi, *Adv. Colloid Interface Sci.*, 2020, **278**, 102126.

36 B. Huang, *Biomanufacturing Reviews*, 2020, **5**, 1–26.

37 B. Ernould, O. Bertrand, A. Minoia, R. Lazzaroni, A. Vlad and J. F. Gohy, *RSC Adv.*, 2017, **7**, 17301–17310.

38 T. Fujigaya and N. Nakashima, *Sci. Technol. Adv. Mater.*, 2015, **16**(2), 024802.

39 S. H. Park, K. Ogino and H. Sato, *Polym. Adv. Technol.*, 2000, **11**, 349–358.

40 A. F. Fehervari, L. C. Kagumba, S. Hadjikyriacou, F. Chen and R. A. Gaudiana, *J. Appl. Polym. Sci.*, 2002, **87**, 1634–1645.

41 J. H. Sim, K. Yamada, S. H. Lee, S. Yokokura and H. Sato, *Synth. Met.*, 2007, **157**, 940–944.

42 T. K. Gupta, B. P. Singh, S. R. Dhakate, V. N. Singh and R. B. Mathur, *J. Mater. Chem. A*, 2013, **1**, 9138–9149.

43 W. J. Xu, H. Z. Chen, M. M. Shi, Y. G. Huang and M. Wang, *Nanotechnology*, 2006, **17**, 728–733.

44 Z. Spitalsky, D. Tasis, K. Papagelis and C. Galiotis, *Prog. Polym. Sci.*, 2010, **35**, 357–401.

45 K. Y. Chiu, T. X. Su, J. H. Li, T. H. Lin, G. S. Liou and S. H. Cheng, *J. Electroanal. Chem.*, 2005, **575**, 95–101.

46 M. E. Ghica, G. M. Ferreira and C. M. A. Brett, *J. Solid State Electrochem.*, 2015, **19**, 2869–2881.

47 T. S. Mathis, N. Kurra, X. Wang, D. Pinto, P. Simon and Y. Gogotsi, *Adv. Energy Mater.*, 2019, **9**, 1–13.

48 P. Simon, Y. Gogotsi and B. Dunn, *Science*, 2014, **343**, 1210–1211.

49 X. Yang and A. L. Rogach, *Adv. Energy Mater.*, 2019, **9**, 1–10.

50 X. Li and B. Bhushan, *Mater. Charact.*, 2002, **48**, 11–36.

51 P. V. Pavoor, B. P. Gearing, R. E. Gorga, A. Bellare and R. E. Cohen, *J. Appl. Polym. Sci.*, 2004, **92**, 439–448.

52 M. Olek, K. Kempa, S. Jurga and M. Giersig, *Langmuir*, 2005, **21**, 3146–3152.